Article

Benchmark of Popular Free Energy Approaches Revealing the Inhibitors Binding to SARS-CoV-2 Mpro

Son Tung Ngo,* Nguyen Minh Tam, Minh Quan Pham, and Trung Hai Nguyen

Cite This: https://doi.org/10.1021/acs.jcim.1c00159

Read Online

ACCESS | 📊 Metrics & More | 📰 Article Recommendations | 🅂🄸 Supporting Information

ABSTRACT: The COVID-19 pandemic has killed millions of people worldwide since its outbreak in December 2019. The pandemic is caused by the SARS-CoV-2 virus whose main protease (Mpro) is a promising drug target since it plays a key role in viral proliferation and replication. Currently, developing an effective therapy is an urgent task, which requires accurately estimating the ligand-binding free energy to SARS-CoV-2 Mpro. However, it should be noted that the accuracy of a free energy method probably depends on the protein target. A highly accurate approach for some targets may fail to produce a reasonable correlation with the experiment when a novel enzyme is considered as a drug target. Therefore, in this context, the ligand-binding affinity to SARS-CoV-2 Mpro was calculated via various approaches. The molecular docking approach was manipulated using Autodock Vina (Vina) and Autodock4 (AD4) protocols to preliminarily investigate the ligand-binding affinity and pose to SARS-CoV-2 Mpro. The binding free energy was then refined using the fast pulling of ligand (FPL), linear interaction energy (LIE), molecular mechanics-Poisson−Boltzmann surface area (MM-PBSA), and free energy perturbation (FEP) methods. The benchmark results indicated that for docking calculations, Vina is more accurate than AD4, and for free energy methods, FEP is the most accurate method, followed by LIE, FPL, and MM-PBSA (FEP > LIE ≈ FPL > MM-PBSA). Moreover, atomistic simulations revealed that the van der Waals interaction is the dominant factor. The residues *Thr26, His41, Ser46, Asn142, Gly143, Cys145, His164, Glu166,* and *Gln189* are essential elements affecting the binding process. Our benchmark provides guidelines for further investigations using computational approaches.
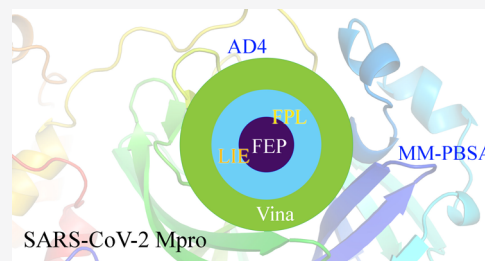
INTRODUCTION

SARS-CoV-2, a novel coronavirus, causes severe acute respiratory syndromes and is responsible for millions of deaths worldwide since its first outbreak in December 2019 in Wuhan, Hubei Province, China.[1−4] The virus has been thought to originate from bats and can quickly transfect between humans.[5] The spreading speed is high since it is able to exist in aerosol especially.[6] Despite the efforts to limit the spread of the virus, more than 80 million people were infected within a year. The outbreak of the virus effectuates the COVID-19 pandemic. Therefore, the development of an effective therapy is thus much more urgent for community health. Although remdesivir was first approved as the anti-viral drug for treating COVID-19,[7] it is probably considered a controversial decision[8] since the drug showed disappointing trials.[9,10] Searching an appropriate treatment for COVID-19 is accordingly a matter of great urgency.

The coronavirus genome sequence, encoding more than 20 different proteins, is known as the largest RNA virus sequence, which is approximately 26−32 kb in length.[11,12] The SARS-CoV-2 virus forms >82% homologous RNA genomes to SARS-CoV.[1] The SARS-CoV-2 main protease (Mpro), being more than 96% identical to SARS-CoV Mpro, is one of the most pivotal proteins because of its direct involvement with viral replication and proliferation.[12,13] In particular, SARS-CoV-2 Mpro splits 11 polyproteins into polypeptides, which are used for replication and to encapsulate a new virus.[12] Several probes in both computational and experimental studies were used to develop an effective therapy and preliminary results were acquired;[14−18] however, as mentioned above, it was a controversial decision,[8] and moreover, an effective drug inhibiting SARS-CoV-2 Mpro is still unattainable.

Currently, computer-aided drug design (CADD) is routinely employed to rapidly screen probable inhibitors for preventing the biological function of a specific enzyme.[19,20] The time and cost for the development of a therapy thus decrease. In particular, the Gibbs free energy difference of the noncovalent chemical reaction between SARS-CoV-2 Mpro and its inhibitors, ΔG, can commonly be computed using molecular dynamics (MD) simulations because it connects with the inhibition constant, K_i, an important metric disclosing the binding process among biomolecules. Reliable calculation of ΔG is one of the most pivotal issues in CADD.[21−23] Therefore, numerous approaches have been developed to resolve the

problem.[23] In order to screen a large number of candidates, which can be up to several million compounds, the computational probe is usually operated via two steps: initial screening of thousands/millions of compounds via rapid protocols such as quantitative structure–activity relationship,[24] molecular docking,[25] and machine learning;[26] ΔG was then realized using MD simulations, in which the popular free energy estimation approaches include the linear interaction energy (LIE),[27] fast pulling of ligand (FPL),[28] molecular mechanism-Poisson–Boltzmann (generalized Born) surface area (MM-PB(GB)SA),[29,30] nonequilibrium molecular dynamics (NEMD),[31] thermodynamic integration,[32] free energy perturbation (FEP) approaches,[33] and so forth. However, it should be noted that the precision and accuracy of the ligand-binding affinity approaches somehow depend on the enzyme targets.[34−40] Therefore, in this work, we benchmarked the performance of docking protocols involving Vina[25] and AD4[41] applying on the SARS-CoV-2 target. Consequently, MD simulations were then performed to investigate the dynamics of the SARS-CoV-2 + inhibitor complexes. The relaxed complexes were then used as initial conformations for probing ligand-binding affinity using four free energy schemes including FPL,[28] LIE,[27] molecular mechanics-Poisson–Boltzmann surface area (MM-PBSA),[32,33] and FEP.[33] The obtained observations probably guide for further investigations using computational approaches.

MATERIALS AND METHODS

Structure of the Receptor and Ligands. The X-ray diffraction structure of SARS-CoV-2 Mpro was obtained from the Protein Data Bank (PDB) with the PDB ID 7JYC.[42] The structure of 34 ligands was taken from the PubChem database[43] referring to the previous work,[44−51] and their 2D structure is reported in Table S1 in the Supporting Information.

Molecular Docking Simulations. Vina[25] and AD4[41] were manipulated to dock the available inhibitors to the binding cleft of SARS-CoV-2 Mpro. The binding cleft was selected as the binding region of the compound named narlaprevir.[42] In particular, the grid size for docking was chosen as 24 × 24 × 24 Å according to the previous work.[16,17] The modeling of docking simulations is described in Figure 1A.

Autodock Vina (Vina).[25] The performance of Vina depends on the parameter's exhaustiveness, which was chosen to be 8.[34,52] The largest energy difference between docking shapes was set to 7 kcal mol^{-1}. The largest ligand-binding affinity was selected as the best docking structure.

Autodock4 (AD4).[41] AD4 was used with a grid size of 72 × 72 × 72 Å and with a spacing of 0.333 Å. Autogrid4 was selected to perform the docking. The inhibitor was docked to SARS-CoV-2 Mpro with a genetic algorithm (GA) run of 10, a population size of 150, and a number of 27 000 generations. The GA number of evaluations was 250 000. The lowest binding free energy cluster was selected as the best docking conformation.

MD Simulations. MD simulations were performed to improve the docking results of the available inhibitors to SARS-CoV-2 Mpro by using GROMACS version 5.1.5.[53] In particular, SARS-CoV-2 Mpro and neutralized ions were described via the Amber99SB-iLDN force field.[54] The TIP3P water model was simultaneously used to represent water molecules.[55] The protonation states of the protein were predicted by GROMACS using canonical pK_a values in a
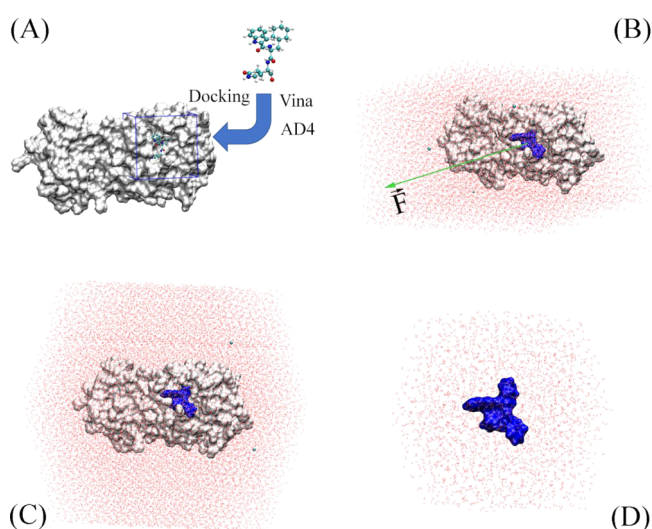
Figure 1. Computational scheme via molecular docking, steered molecular dynamics (SMD), and MD simulations. (A) Modeling of molecular docking simulations. Inhibitors were docked to the binding cleft of SARS-CoV-2 Mpro, which was limited in the docking box with a volume of ca. 13.82 nm^3. (B) Starting structure of the SARS-CoV-2 Mpro + inhibitor complex for estimating the ligand-binding affinity via the FPL scheme. (C) Initial shape of the SARS-CoV-2 Mpro + inhibitor complex for MD simulations. (D) Starting conformation of the solvated inhibitor. The cyan balls describe the neutralized Na$^+$ ions.

neutral solution since it probably adjusts the ligand-binding free energy,[56] in which the protonation state of the catalytic dyad including His41 and Cys145 was also predicted (cf. Figure S1 in the Supporting Information). The most possible distance between the His41Hε atom and Cys145Sγ is ca. 0.44 nm (Figure S1A), which is in good agreement with the experimental data.[42] Consequently, the inhibitor was illustrated using a general Amber force field[57] with the help of AmberTools18 and ACPYPE packages.[58,59] It should be noted that before parameterizing the ligand, the quantum chemical calculation using the B3LYP functional at the 6-31G(d,p) level of theory was performed to obtain chemical information of the inhibitor during which the restrained electrostatic potential (RESP) approach was used to assign atomic charges upon quantum simulations using an implicit solvent environment, $\varepsilon = 78.4$.[57] Moreover, the SARS-CoV-2 Mpro + inhibitor complex was placed into a rectangular or dodecahedron periodic boundary (PBC) condition box with a volume of 506 or 820 nm^3 corresponding to SMD (Figure 1B) or unbiased MD (Figure 1C) simulations, respectively. The soluble system hence encompasses ca. 50,000 or 80,000 atoms, respectively, involving SARS-CoV-2 Mpro, ligands, water molecules, and neutralized Na$^+$ ions. Moreover, in order to carry out the perturbation simulations, the ligand was individually simulated in a dodecahedron PBC box with a volume of ca. 85 nm^3 (Figure 1D). The soluble ligand system consists of ca. 8000 atoms, involving ligands, water molecules, and counterbalanced ions.

The parameters for operating MD simulations were described in previous works.[16,17] In particular, the integral was attempted every 2 fs. A nonbonded pair was enumerated within a radius of 0.9 nm. The van der Waals (vdW) interaction was assessed using the cutoff scheme, while the electrostatic (cou) interaction was determined via the fast

Table 1. Calculated Results in Comparison with the Experimental Values of Some Compounds to SARS-CoV-2 Mpro

no	name	ΔG_{Vina}	ΔG_{AD4}	W	ΔG_{LIE}	$\Delta G_{MM\text{-}PBSA}$	ΔG_{FEP}	ΔG_{EXP}[a]
1	7J[b]	−7.4	−6.0	95.7 ± 6.1	−15.04 ± 0.30	−19.3 ± 1.03	−17.95 ± 2.74	−8.69[44]
2	11a[b]	−7.3	−8.1	109.7 ± 3.1	−14.78 ± 0.81	−29.67 ± 0.30	−18.95 ± 0.52	−9.96[45]
3	11b[b]	−7.4	−8.0	91.3 ± 7.9	−13.99 ± 0.36	−14.41 ± 1.85	−16.53 ± 0.59	−10.13[45]
4	11r	−6.8	−6.9	96.6 ± 8.2	−15.98 ± 1.92	−15.14 ± 1.61	−20.89 ± 0.51	−9.23[46]
5	13a[b]	−7.6	−7.6	64.7 ± 10.6	−10.07 ± 0.59	−0.71 ± 0.87	−10.94 ± 2.51	−7.70[46]
6	13b[b]	−7.7	−7.4	81.3 ± 6.1	−16.16 ± 2.00	−19.93 ± 3.96	−16.47 ± 0.32	−8.45[46]
7	baicalein	−6.8	−5.7	36.5 ± 8.0	−10.36 ± 2.57	−8.88 ± 2.92	−8.40 ± 2.23	−8.25[47]
8	boceprevir[c]	−7.1	−8.8	54.5 ± 1.8	−11.75 ± 0.85	−9.74 ± 0.48	−7.65 ± 1.31	−7.37[48]
9	calpain inhibitor I	−5.3	−5.4	50.2 ± 4.9	−10.77 ± 0.87	−7.51 ± 0.17	−6.41 ± 0.37	−6.94[48]
10	calpain inhibitor II[c]	−5.6	−5.3	74.1 ± 22.9	−12.21 ± 0.22	−14.92 ± 6.95	−9.09 ± 2.39	−8.23[48]
11	calpain inhibitor XII[c]	−6.3	−5.1	51.8 ± 5.7	−11.98 ± 0.30	−24.73 ± 1.21	−9.27 ± 0.88	−8.69[48]
12	calpeptin	−4.9	−6.1	33.0 ± 5.4	−9.75 ± 1.07	−4.37 ± 1.89	−3.43 ± 0.97	−6.81[48]
13	carmofur[b]	−5.6	−6.0	39.1 ± 5.9	−9.30 ± 1.78	−3.97 ± 0.98	−7.12 ± 3.20	−7.86[49]
14	GC-373[b]	−7.2	−6.6	53.1 ± 8.3	−12.16 ± 0.41	−12.04 ± 1.13	−10.32 ± 1.55	−8.76[50]
15	MG-115	−6.1	−5.4	57.8 ± 2.2	−11.34 ± 0.57	−8.14 ± 1.21	−9.19 ± 0.73	−7.53[48]
16	MG-132[c]	−6.2	−5.2	71.4 ± 9.1	−11.50 ± 0.39	−12.13 ± 3.06	−8.48 ± 0.41	−7.41[48]
17	narlaprevir[b]	−7.5	−5.9	69.9 ± 2.1	−12.69 ± 0.05	−22.75 ± 0.25	−6.57 ± 0.50	−7.18[48]
18	PX-12[b]	−3.9	−4.8	32.1 ± 1.0	−8.67 ± 0.05	−32.44 ± 0.73	−2.56 ± 0.30	−6.39[49]
19	shikonin	−6.1	−6.0	27.3 ± 6.9	−9.37 ± 0.27	−0.74 ± 4.30	−3.01 ± 0.95	−6.58[49]
20	tideglusib	−6.6	−7.1	36.5 ± 3.1	−9.92 ± 0.27	−10.56 ± 2.93	−4.26 ± 0.12	−7.95[49]

[a]The experimental binding free energies were gained based on the IC_{50} value, approximating that the one equals to the inhibition constant K_i and based on the assumption of the contribution of the covalent binding energy is small. [b]The covalent binding inhibitors. [c]The possible slow covalent binding inhibitors. The unit is kcal mol⁻¹.

particle mesh Ewald electrostatics scheme.[60] The solvated system was initially minimized via the steepest descent approach. The canonical (NVT) and isobaric−isothermal (NPT) simulations, with lengths of 0.1 and 2.0 ns, respectively, were then followed to equilibrate the system. The final conformations of NPT simulations of the solvated complex were operated as the initial structure of SMD or MD simulations, a length of 0.5 or 20.0 ns, respectively. Moreover, the solvated inhibitor system was run for 5.0 ns. Each system was imitated two times for getting better samples.

Free Energy Calculations. *FPL Scheme.* An externally harmonic force was applied to dissociate the inhibitor from the SARS-CoV-2 Mpro binding cleft as mentioned in the Supporting Information. In particular, cantilever spring constant, v = 600 kJ mol⁻¹ nm⁻², and pulling velocity, k = 0.005 nm ps⁻¹, were selected as forced parameters.[28] During SMD simulations, the pulling work, W, was recorded to be used as a critical factor to estimate the ligand-binding affinity[28] since it correlates with the binding free energy, ΔG, via the isobaric−isothermal Jarzynski equality.[61] The pulling work W is calculated as follows

$$W = v \int_0^t F(t)\,dt \tag{1}$$

LIE Calculation. The ligand-binding free energy, ΔG_{LIE}, was computed as the mean of vdW and cou interaction differences of the inhibitor with its neighboring atoms upon incorporation, that is, the individual ligand in the solvent (unbound state—denoted as subscript u) and the inhibitor in the binding mode with SARS-CoV-2 Mpro (bound state—denoted as subscript b). The formula of the LIE approach can be expressed as follows

$$\Delta G_{LIE} = \alpha(\langle V_{l-s}^{vdW}\rangle_b - \langle V_{l-s}^{vdW}\rangle_u) + \beta(\langle V_{l-s}^{cou}\rangle_b - \langle V_{l-s}^{cou}\rangle_u) + \gamma \tag{2}$$

The coefficient γ, a constant, is associated with the alteration of the hydrophobic nature of the binding cleft conceding to various species of inhibitors, whereas the coefficients α and β are rating parameters for nonpolar and polar interactions, respectively.[62] Additional information about the LIE approach is described in the Supporting Information.

MM-PBSA Analysis. The ligand-binding affinity, $\Delta G_{MM\text{-}PBSA}$, can be assessed using MD simulations via the MM-PBSA approach[29,30] as follows

$$\Delta G_{MM\text{-}PBSA} = \Delta E_{cou} + \Delta E_{vdW} + \Delta G_{sur} + \Delta G_{PB} - T\Delta S \tag{3}$$

where ΔE_{cou}, ΔE_{vdW}, ΔG_{sur}, and ΔG_{PB} correspond to the energetic changes in cou, vdW, nonpolar, and polar interactions, respectively; $T\Delta S$ is the entropic contribution to $\Delta G_{MM\text{-}PBSA}$. In particular, ΔE_{cou} and ΔE_{vdW} were computed using GROMACS tools "gmx energy". The nonpolar metrics, ΔG_{sur}, was determined via the Shrake−Rupley formula,[63] which is $\Delta G_{sur} = \gamma SASA + \beta$, where γ = 0.0072 kcal mol⁻¹ Å⁻² and β = 0.[64] The polar component, ΔG_{PB}, was assessed by numerically resolving the Poisson−Boltzmann equation using an implicit solvent model.[65,66] Finally, the entropic term can be probed via normal mode approximation.[67] Additional information about the MM-PBSA approach is described in the Supporting Information.

Double-Annihilation Binding Free Energy Investigation. The inhibitor was changed from *bound* state to *unbound* state by using λ-alteration simulations,[68] which concur at λ = 0 and λ = 1. Several values of the coupling parameter λ were used to complete this task. The free energy change, $\Delta G_{\lambda=0\to1} = -k_B T\ln\langle e^{-\Delta H/k_B T}\rangle_{\lambda=0}$, corresponds to the work of the ligand annihilation process, whose information is described in detail in the Supporting Information. The value can be assessed via the Bennett acceptance ratio scheme.[69] The binding free energy between SARS-CoV-2 Mpro and the inhibitor, ΔG_{FEP}, is thus obtained due to the difference of the free energy

changes upon two ligand annihilation processes involving a demolishing inhibitor in the solvated complex, $\Delta G_{\lambda=0\rightarrow1}^{Comp}$, and an inhibitor, $\Delta G_{\lambda=0\rightarrow1}^{lig}$,[22] as follows

$$\Delta G_{FEP} = \Delta G_{\lambda=0\rightarrow1}^{Comp} - \Delta G_{\lambda=0\rightarrow1}^{lig} \tag{4}$$

Analysis Tools. Because the protonation states of ligands possibly alter the protein−ligand binding,[70] the chemicalize webserver, a tool of ChemAxon, was used to assess the protonation states of inhibitors. The Adaptive Poisson-Boltzmann Solver (APBS) webserver was used to determine the surface charge of the protease.[66,71] The correlation error was calculated using 1000 rounds of the bootstrapping method.[72] The intermolecular nonbonded contact (NBC) between the ligand atoms and the residual SARS-CoV-2 Mpro was confirmed when the pair between their nonhydrogen atoms is smaller than 4.5 Å. The intermolecular hydrogen bond (HB) between the Mpro residues and the inhibitors was endorsed when the angle ∠ acceptor (A)-hydrogen (H)-donor (D) is larger than $3\pi/4$ and the pair A−D is smaller than 3.5 Å. ROC-AUC was calculated using the Scikit-Learn library.[73] Since ROC-AUC calculations require ligands to be assigned a binary label, we classify the ligands according to their experimental binding affinity and split them into two halves. The ligands in the first half having experimental binding free energy below the median were assigned the *strong binder* label, whereas those in the second half were assigned the *weak binder* label. ROC-AUC was used to benchmark different computational methods in terms of discriminating between strong and weak binders.

■ RESULTS AND DISCUSSION

Molecular Docking Calculations. The obtained results are shown in Tables 1 and S1 in the Supporting Information. Initially, we assessed the docking results against the relevant experimental data including binding affinity and native binding poses.[44−50] The assessment includes two parts: correlation between docking and experimental ligand-binding affinity and successful docking rate.[34] The estimated correlation coefficients for Vina and AD4 are $R_{Vina} = 0.60 \pm 0.13$ and $R_{AD4} = 0.47 \pm 0.21$, respectively. This indicates that the docking energies of Vina are more strongly correlated with experiments than those of AD4. Moreover, the root-mean-square error (RMSE) of Vina is lower than that of AD4, that is, $RMSE_{Vina} = 1.78 \pm 0.17$ and $RMSE_{Vina} = 1.97 \pm 0.17$ kcal mol^{-1}, respectively. Although AD4 required much more computing resources than Vina does, its docking performances lagged behind Vina. It is probably caused by the difference in scoring functions as indicated by prior observations,[34] in which AD4 uses a hybrid physical-based/empirical scoring function, while Vina uses an empirical scoring function.[25,41] Furthermore, in the previous work,[74] AD4 gave poor correlation, $R = 0.36$, with $\Delta G_{Jarzynski}$, which is obtained via NEMD simulations,[31] a much more accurate free energy approach. Therefore, it may be argued that Vina is the appropriate protocol for preliminary assessment of the ligand-binding affinity to SARS-CoV-2 Mpro.

The inhibitor-binding pose was also obtained using this process. The docking pose forms a small root-mean-square deviation (RMSD) with respect to the experimental pose. It was considered as a successfully docked conformation if the RMSD is smaller than 2 Å.[34] In particular, nine compounds including 7j, 11a, 11b, 13b, *baicalein, boceprevir, calpeptin,* GC-

373, and *narlaprevir* were reported to have the experimental binding poses with the PDB IDs 6XMK,[44] 6LZE,[45] 6M0K,[45] 6Y2F,[46] 6M2N,[47] 7K40,[42] 7AKU,[75] 6WTK,[50] and 7JYC,[42] respectively. Over these systems, the successful docking rate of Vina is ca. 67% with a mean RMSD of 1.97 ± 0.32 Å, as presented in Figure 2. It is significantly better than those by
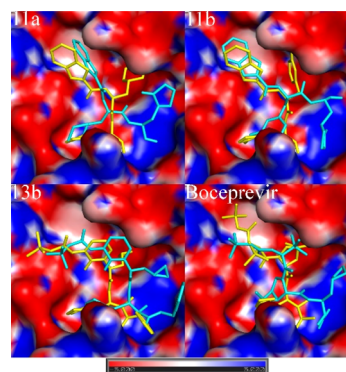
Figure 2. Comparison of docking (cyan) and experimental binding (yellow) poses of 11a, 11b, 13b, and boceprevir to SARS-CoV-2 Mpro. The surface charge, ranging from −5 to 5, of the protease was computed via the APBS webserver. The docking results were obtained by using the Vina package.

AD4 with the RMSD between docked and experimental structures of 3.22 ± 0.33 Å, as represented in Figure S2 in the Supporting Information. Therefore, it may be concluded that Vina not only formed the proper affinity results but also showed the suitable binding pose to SARS-CoV-2 Mpro.

MD Simulations. Because the molecular docking simulations often use many constraints/approximations to accelerate the calculation speed, the results often need to be refined using more accurate protocols.[17,18] In this context, because Vina formed the most suitable binding affinity and pose as discussed above, we have chosen the docking structures provided by this approach as initial structures for simulating via SMD/MD techniques. The ligand-binding free energy calculation methods were thus carried out.[23,35] The performance of free energy calculations based on SMD/MD trajectories was thus assessed.

Steered MD Simulation. FPL is an efficient technique to quickly classify the ligand-binding affinity.[28] This approach successfully estimated the affinities of several inhibitors binding to SARS-CoV-2 Mpro, which suggested a shortlist of potent compounds to further evaluate via perturbation simulations.[16] A benchmark with 11 compounds was then used later on, indicating that the correlation coefficient of the pulling work, W, and the experimental binding free energy, ΔG_{EXP}, are appropriate with a value of $R_{FPL} = -0.76 \pm 0.10$.[17] However, due to the small size of the testing set, the obtained results are probably unstable due to the large value of the computed error. Consequently, the value did not show superiority over Vina docking with $R_{Vina} = 0.72 \pm 0.14$, which is within the computed error.[17] In this context, we benchmarked again this approach for evaluating the ligand-binding affinity versus SARS-CoV-2 Mpro with a larger testing set. The FPL scheme was thus used for refining the obtained docking results, which were provided by Vina. In FPL simulations, an externally pulling force was applied to extract inhibitors from *bound* to *unbound* states. The recorded rupture force, F_{max}, and pulling work, W, during the simulations are given in Table S2 in the

Supporting Information. The F value in time dependence is also shown in Figure S3 in the Supporting Information. The average of W values falls in the range 18.3 ± 1.4 to 111.3 ± 6.0 kcal mol^{-1}, providing a median of 56.0 ± 5.0 kcal mol^{-1}, while the mean rupture force F_{max} is within the range from 279.5 ± 12.7 to 1040.6 ± 68.9 pN, giving a median of 581.9 ± 41.2 pN. The ligand-binding affinity is possibly ranked via the W value, which formed an appropriate correlation, $R = -0.51 \pm 0.15$ (cf. Table S2), with the respective experiments.[44−50] The obtained coefficient indicated that FPL is significantly worse than Vina docking, $R_{Vina} = 0.60 \pm 0.13$, in predicting the ligand-binding affinity of SARS-CoV-2 Mpro. The poorly correlated outcomes of FPL probably appear due to SMD simulations performed using the conformations provided by the short NPT simulations, which may not be sufficient to reach the equilibrium states. Therefore, the unbiased MD simulations with a length of 20 ns were performed after NPT simulations and were reported below. We used the last conformations of MD simulations as starting structures of FPL calculations. The obtained outcomes are reported in Tables 1 and S3 in the Supporting Information, in which the F value during SMD simulations is reported in Figure S4 in the Supporting Information. The F_{max} and W values were thus altered and ranged from 342.0 to 961.4 pN and 27.3 to 109.7 kcal mol^{-1}, forming median values of 644.0 ± 39.2 pN and 61.3 ± 5.3 kcal mol^{-1}, respectively. The obtained correlation between W and ΔG_{EXP} was thus increased from $R = -0.51 \pm 0.15$ to $R_{FPL} = -0.74 \pm 0.11$ (cf. Figure 3). The FPL technique is thus able to improve upon the docking results; however, the equilibrated simulations are required to be performed carefully.
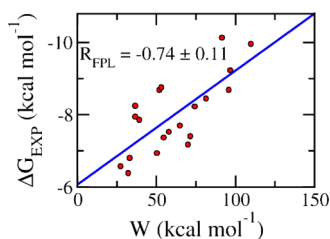
Figure 3. Association of pulling work W and ΔG_{EXP}. The W values were calculated via eq 1. The ΔG_{EXP} values were computed when the half-maximal inhibitory concentration, IC$_{50}$, was assumed to be equal to the inhibition constant, K_i.

Unbiased MD Simulations. As mentioned above, the FPL results based on the rather short relaxation time of only 2 ns were probably limited since it may not be sufficient to reach the equilibrium states. Moreover, the SARS-CoV-2 Mpro C$_\alpha$ atoms were restrained, probably hindering the structural change of the complexed system to equilibrium states. The complexed conformation including SARS-CoV-2 Mpro and the ligand in the best docking pose provided by Vina was thus solvated and equilibrated via unbiased MD simulations with a length of 20 ns. The accuracy of the following FPL calculations was thus increased significantly (Figure 3). During the unbiased MD simulation, the complexes almost reached the equilibrium states after 5 ns (cf. Figure S5 in the Supporting Information). Furthermore, the all-atom RMSD of SARS-CoV-2 Mpro was found to be in good agreement with the previous work[76] (cf. Figure S6 in the Supporting Information). Therefore, the snapshots over an interval of 10−20 ns with a stride of 10 ps were collected for binding free energy

calculation via the LIE and MM-PBSA approaches. In addition, the structures extracted from MD trajectories of 2.5−5 ns of the solvated inhibitor system were also involved in free energy calculations via the LIE approach.

In order to probe the factors controlling the binding process of inhibitors to Mpro, the intermolecular NBC and HB between inhibitors and individual residues of SARS-CoV2 Mro were investigated using equilibrium snapshots of all complexes. The obtained outcomes are presented in Figure S7 in the Supporting Information, which mentioned 30 residues establishing NBC to inhibitors over more than 15% of the appraised shapes (40,000 snapshots totally). However, there are only 19/30 residues that created HB to inhibitors. Shortening the list, we have only counted residues, which simultaneously showed NBC and HB to inhibitors with a probability being higher than 42 and 4%, respectively. It should be noted that 47 ± 5 and $6 \pm 2\%$ amounts correspond to the averaged values over 30 residues. Nine residues were obtained and are described in Figure 4. We may argue that the residues
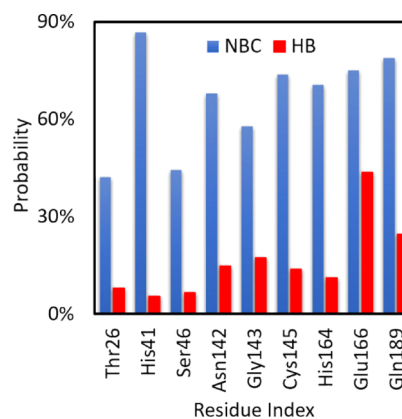
Figure 4. Critical residues forming NBC and HB to the inhibitors. The results were obtained over the equilibrium snapshots of MD simulations of all complexes.

Thr26, His41, Ser46, Asn142, Gly143, Cys145, His164, Glu166, and *Gln189* are critical elements governing the binding process of ligands to SARS-CoV-2 Mpro. The large contribution of these residues to the ligand-binding process implies that the protonation state of these residues involving the catalytic dyad probably alters the ligand-binding affinity. Therefore, the issue should be carefully carried out in further work. Furthermore, possible mutations at these residues could change much the ligand-binding free energy to SARS-CoV-2 Mpro.

In addition, the clustering method was then applied to characterize the structural change of nine critical residues during the equilibrium conformations of all complexes. The calculation was performed with a nonhydrogen atomic RMSD cutoff of 1.2 Å over 40 000 structures of nine residues in stabilizing *bound* states with 20 inhibitors. One cluster was found, which is shown as colorful residues in Figure 5. The representative structure of nine critical residues was compared with the starting conformation, which is in gray color. The differences between the MD refined and starting structures are noted as red arrows in Figure 5. The significant structural changes are the flexing of the residue *Asn142* and the rotation of the hydroxyl and thiol side chains of *Ser46* and *Cys145*, respectively. The side chain residues probably rotate to form HB to inhibitors. Moreover, overall, the difference between the
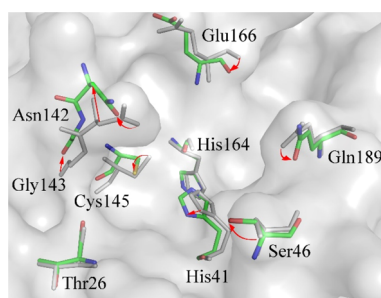
Figure 5. Representative structures of nine critical residues via the nonhydrogen RMSD clustering calculation with a cutoff of 1.2 Å. The colorful residues represent the MD refined structure in comparison with the initial structure, which is denoted in gray color. Red arrows imply the change of these residues during MD simulations.

representative structure and the initial conformation is ca. 1.0 Å, implying the stability of the SARS-CoV-2 Mpro active site during MD simulations.

Binding Free Energy Calculation by Using the LIE Scheme. The difference between the averaged vdW and cou interaction energies between each inhibitor to SARS-CoV-2 Mpro, *bound* state, and the solution, *unbound* state, as long as ΔG_{EXP} is given in Tables 1 and S4 in the Supporting Information. The binding free energy, ΔG_{LIE}, is computed using eq 2. Traditionally, the parameters α and β were chosen as 0.18 and 0.50, respectively.[27,77] However, similar to the Aβ oligomeric system,[78] no correlation, $R = -0.13 \pm 0.20$, was observed between the calculated and experimental values. This is probably due to the shallow binding cleft of SARS-CoV-2 Mpro, which is similar to the ligand−surface binding in the case of Aβ oligomer.[78] Therefore, the parameters including $\alpha = 0.288$, $\beta = -0.049$, and $\gamma = -5.880$ of the Aβ system[78] were proposed to be used for calculating the ligand-binding free energy of the SARS-CoV-2 Mpro + inhibitor complex. Interestingly, the set of parameters gave a correlation coefficient $R_{LIE} = 0.73 \pm 0.09$ and RMSE = 4.12 ± 0.40 kcal mol^{-1} (Figure 6). Absolutely, the LIE approach formed similar
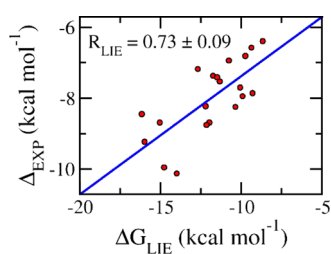
Figure 6. Comparison of ΔG_{LIE} and ΔG_{EXP}. The calculated binding free energy was computed using eq 2 with the parameters $\alpha = 0.288$, $\beta = -0.049$, and $\gamma = -5.880$ referring the Aβ oligomer + inhibitor complex. The ΔG_{EXP} values were computed when the half-maximal inhibitory concentration, IC$_{50}$, was assumed to be equal to the inhibition constant, K_i.

accuracy outcomes, $R_{LIE} = 0.73 \pm 0.09$, compared to FPL simulations, $R_{FPL} = -0.74 \pm 0.11$. Moreover, the negative parameter β may imply the loss of cou interactions of inhibitors upon association (cf. Table S4) or it may be argued that the vdW interactions control the binding process of inhibitors to the protease. It is in good agreement with the previous outcomes[16,18] and obtained results via MM-PBSA and perturbation calculations below. Furthermore, the negative

value γ implies that the hydrophobic interactions between inhibitors and SARS-CoV-2 Mpro are strong as mentioned in the conclusion about the superiority of the above vdW term. In addition, although the LIE showed a good Pearson correlation, ΔG_{LIE} overestimates ΔG_{EXP} with an amount of ca. 3.89 kcal mol^{-1} (see Table 1). It is probably caused by the lower hydrophobic interaction between the SARS-CoV-2 Mpro + inhibitor complexes compared with the Aβ-complexed system or the incorrect imitation of the interaction between inhibitors and the surrounding atoms.[79,80] Overall, it may be argued that the binding process of the SARS-CoV-2 Mpro + inhibitor complex is similar to the Aβ oligomer + ligand complex, but the hydrophobic contacts of the Mpro complex are weaker than the Aβ ones.

Establishing the Ligand-Binding Free Energy via the MM-PBSA Protocol. The equilibrium conformations of the SARS-CoV-2 Mpro + inhibitor complex during MD simulations were implemented for estimating the binding free energy using continuum models[29,30] following eq 3. It should be highlighted that our group has successfully calculated the ligand-binding free energy for various biomolecules using the MM-PBSA method.[78,81−83] The obtained outcomes are described in Tables 1 and S5 in the Supporting Information. In particular, $\Delta G_{MM-PBSA}$ overestimates ΔG_{EXP} with a value of ca. 5.60 kcal mol^{-1}, which is slightly larger than that given by the LIE protocol. Moreover, the MM-PBSA method provides a poor accuracy in comparison with the corresponding experiments, $R_{MM-PBSA} = 0.32 \pm 0.29$ and RMSE = 10.15 ± 1.92 kcal mol^{-1} (Figure 7). It is in good agreement with the previous study[84]
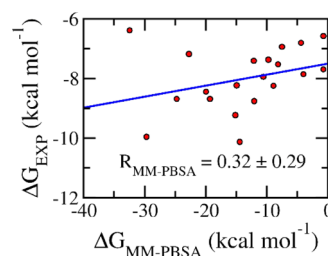
Figure 7. Comparison of $\Delta G_{MM-PBSA}$ and ΔG_{EXP}. The calculated binding free energy was computed using eq 3. The ΔG_{EXP} values were computed when the half-maximal inhibitory concentration, IC$_{50}$, was assumed to be equal to the inhibition constant, K_i.

that MM-PBSA formed a correlation with the experiment with a value of $R_{MM-PBSA} = 0.25$ upon investigating 15 complexes. Interestingly, as mentioned above that the binding process of inhibitors to SARS-CoV-2 Mpro is quite similar to that of the inhibitors to the Aβ oligomer, the Pearson correlations of two systems are similar, $R_{MM-PBSA}^{SARS-CoV-2} = 0.32$ versus $R_{MM-PBSA}^{A\beta} = 0.27$.[78] The poor accuracy of the MM-PBSA approach applying on SARS-CoV-2 Mpro is possibly similar to the Aβ system that is probably caused by the selection of an inappropriate dielectric constant, ε, and roughly entropic approximation.[35,78,85] Furthermore, the ε issue was also consolidated via the inhibitor interaction diagram analysis (cf. Table S2 in the Supporting Information) where the solvation exposure of inhibitors is absolutely complicated. Therefore, further investigation to characterize factors affecting the accuracy of MM-PBSA applying on SARS-CoV-2 Mpro should be performed before the approach is widely used for screening potential inhibitors for the Mpro target.

Determination of Ligand-Binding Free Energy Using the FEP Method. In recent reports,[18,84] the FEP simulation successfully determined the ligand-binding free energy and is known as the most accurate free energy method.[23,86] However, although the perturbation results correlate with the respective experiments,[18,84] the Pearson coefficient diffused in a large range from 0.54 to 0.94. In particular, FEP simulations determined the ligand-binding free energy of 11 inhibitors to SARS-CoV-2 Mpro with high accuracy, $R_{FEP} = 0.94 \pm 0.04$.[18] In a different study, perturbation simulations also formed a Pearson correlation $R_{FEP} = 0.54$ when 15 complexes were considered.[84] Therefore, in this work, we benchmarked the FEP performance on a larger set from multi-sources, which would probably provide a clarification for the accomplishment of this approach.

The final structures of MD simulations mimicking the solvated complex and ligand were utilized as the input of λ-alteration simulations. The obtained results are reported in detail in Tables 1 and S6 in the Supporting Information. The perturbation simulations provide the highest accuracy results with a Pearson correlation of $R_{FEP} = 0.85 \pm 0.06$ (cf. Figure 8).
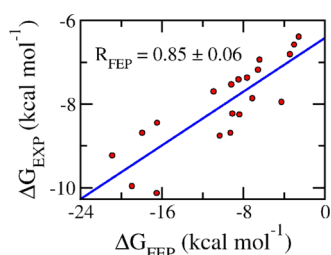
Figure 8. Comparison of ΔG_{FEP} and ΔG_{EXP}. The calculated binding free energy was computed using eq 4. The ΔG_{EXP} values were computed when the half-maximal inhibitory concentration, IC_{50}, was assumed to be equal to the inhibition constant, K_i.

Although R_{FEP} is quite high, it is far from being perfect. The inaccurate outcomes are probably caused by the insufficient simulating the ligand−covalent binding interaction of conventional MD simulations. Because some covalent and slow covalent binding inhibitors were employed upon investigations as noted in Table 1, the binding free energy of these compounds to SARS-CoV-2 Mpro involves two components including covalent and noncovalent binding free energy.[87] The further expensive computing approach such as QM/MM or PDLD/S-LRA/β should be thus carried out to refine the binding process.[87−89] However, in this work, the computational investigations were limited in the framework of the classical simulation, which is widely used and good enough to estimate the potential inhibitors for Mpro. Moreover, in average over complexes, the ΔG_{FEP} value is -9.87 ± 1.20 kcal mol^{-1}, which overestimates ca. 1.87 kcal mol^{-1} compared to the mean of the experimental values. The difference is significantly smaller than those obtained by LIE, ca. 3.89 kcal mol^{-1}, and MM-PBSA, 5.60 kcal mol^{-1}, methods. The difference between the mean of experimental and computational values probably comes from the incorrect simulations of the interaction between inhibitors and neighboring atoms.[79,80] The rough assumption of the IC_{50} equals the inhibition constant K_i, when calculated the experimental binding free energy, also adopts a shifting possibility. Furthermore, the obtained results by λ-alteration simulations also revealed the binding process of the SARS-CoV-2 Mpro inhibitor. The vdW interaction is dominant in the binding process of ligands to Mpro, which is in good agreement with the previous observations[16,18] because the average values of ΔG_{cou} and ΔG_{vdW} are -2.82 ± 0.83 and -7.05 ± 0.49 kcal mol^{-1}, respectively.

Calculating the Binding Affinities of Other SARS-CoV-2 Inhibitors. The binding free energy of some available SARS-CoV-2 inhibitors to the Mpro was also evaluated using the assessed approaches. The outcomes are described in Tables 2 and S7−S10 and Figures S8 and S9 in the Supporting Information. Although the inhibitory concentration of these compounds was extracted from cell culture experiments,[51] indicating that drug targets probably differ from SARS-CoV-2 Mpro such as RNA polymerase, appropriate correlations between the calculated results and experimental data were recorded. Therefore, it may be argued that there are many compounds aiming at inhibiting Mpro. In particular, in good agreement with the above evaluation, Vina showed the higher correlation, $R_{Vina} = 0.78 \pm 0.23$, compared with the AD4 package, $R_{AD4} = 0.48 \pm 0.23$. The binding poses of these compounds to SARS-CoV-2 Mpro were thus used as the initial

Table 2. Calculated Results in Comparison with the Experimental Values of Some Compounds to SARS-CoV-2

no	name	ΔG_{Vina}	ΔG_{AD4}	W	ΔG_{LIE}	$\Delta G_{MM-PBSA}$	ΔG_{FEP}	ΔG_{EXP}[a]
1	bazedoxifene	−7.5	−8.1	47.4 ± 9.6	−11.12 ± 1.02	−5.13 ± 1.60	−5.25 ± 2.47	−7.48[51]
2	ciclesonide	−7.4	−8.9	55.9 ± 1.9	−12.89 ± 0.47	−11.58 ± 2.80	−9.87 ± 0.40	−7.34[51]
3	digitoxin	−8.1	−8.1	72.5 ± 5.2	−13.22 ± 0.93	−0.92 ± 2.95	−16.19 ± 3.88	−9.09[51]
4	favipiravir	−4.9	−4.9	16.0 ± 1.5	−7.23 ± 0.35	−2.31 ± 1.56	−0.99 ± 0.51	−4.52[51]
5	gilteritinib	−7.5	−8.5	37.7 ± 2.5	−12.15 ± 0.53	−11.55 ± 3.06	−8.02 ± 0.35	−7.08[51]
6	lopinavir	−6.3	−5.1	41.8 ± 5.1	−12.39 ± 1.94	−9.30 ± 3.95	−4.72 ± 2.92	−6.59[51]
7	mefloquine	−6.5	−6.5	45.7 ± 3.0	−10.51 ± 0.16	−9.84 ± 0.06	−3.05 ± 1.36	−7.34[51]
8	mequitazine	−6.6	−7.7	24.6 ± 2.3	−9.33 ± 0.76	−1.98 ± 4.66	−8.88 ± 0.41	−7.03[51]
9	niclosamide	−6.6	−6.3	41.9 ± 6.0	−10.95 ± 0.57	−8.38 ± 1.95	−8.77 ± 0.40	−8.97[51]
10	osajin	−7.0	−7.7	27.6 ± 4.4	−11.45 ± 0.14	−15.26 ± 3.00	−4.15 ± 1.14	−7.41[51]
11	penfluridol	−6.9	−8.0	59.6 ± 0.5	−10.55 ± 0.38	−0.27 ± 3.41	−10.51 ± 1.51	−7.26[51]
12	phenazopyridine	−6.0	−6.0	23.9 ± 3.2	−9.96 ± 0.56	−5.90 ± 2.98	−3.80 ± 0.58	−6.23[51]
13	proscillaridin	−7.6	−7.4	57.8 ± 4.5	−11.85 ± 0.38	−7.32 ± 1.33	−14.56 ± 2.65	−7.79[51]
14	remdesivir	−6.5	−4.5	37.8 ± 3.9	−12.00 ± 0.31	−28.69 ± 2.94	−8.91 ± 5.65	−6.96[51]

[a]The experimental binding free energies were gained based on the IC_{50} value, approximating that the one equals to the inhibition constant K_i. The unit is kcal mol^{-1}.

structures for SMD/MD refined simulations. The Pearson correlations between FEP, LIE, MM-PBSA, and FPL compared with the experimental data are $R_{FEP} = 0.70 \pm 0.16$, $R_{LIE} = 0.67 \pm 0.28$, $R_{MM-PBSA} = 0.00 \pm 0.26$, and $R_{FPL} = -0.71 \pm 0.17$, respectively. The MM-PBSA approach is different from others since it is very weakly correlated with experiments. Moreover, although FEP, LIE, and FPL showed appropriate results, the linear relationship was decreased. The discrepancies occurred since some compounds probably target on the RNA polymerase rather than Mpro.[14]

Area under the ROC Curve—ROC-AUC. The ROC-AUC values for SARS-CoV-2 Mpro inhibitors and other SARS-CoV-2 inhibitors are shown in Tables S11 and S12. ROC-AUC is a commonly used metric to measure the ability of a binary classifier in distinguishing between two labels. The results indicate that for Mpro inhibitors, FEP and LIE are the best classifiers, followed by MM-PBSA, FPL, Vina, and AD4. However, for other SARS-CoV-2 inhibitors, the two docking methods give better ROC-AUC than the binding free energy methods do, except for the FPL method.

CONCLUSIONS

In this context, in order to benchmark which is the appropriate free energy approach for probing the binding free energy of inhibitors to the SARS-CoV-2 Mpro, we have carried out both molecular docking and MD simulations. Vina and AD4 were employed for docking imitations. We have initially demonstrated that the Vina package is better than the AD4 protocol in both predicting the ligand-binding affinity, $R_{Vina} = 0.60 \pm 0.13$, and binding pose of ligands, where the successful docking rate is of ca. 67%, to the SARS-CoV-2 Mpro target. Surprisingly, AD4 produced poorly correlated results with coefficients of $R_{AD4} = 0.47 \pm 0.21$. It should be noted that the poor accuracy of AD4 was also revealed when the docking results were compared with the NEMD simulations, $R = 0.36$.[74]

MD simulations would then be accomplished. The FEP approach provided the most accurate results, $R_{FEP} = 0.85 \pm 0.06$, compared with the respective experiments. Interestingly, the LIE and FPL approaches also formed good correlation coefficients, $R_{LIE} = 0.73 \pm 0.09$ and $R_{FPL} = -0.74 \pm 0.11$, while using significantly lower computing resources compared to FEP, respectively. However, an appropriate relaxed simulation, which is similar to the prepared input for FEP/LIE/MM-PBSA calculations, was required to reach equilibrium states before FPL was carried out. Because the successful docking rate is ca. 67%, the short NPT simulation may not be sufficient to reach the equilibrium states. The MM-PBSA method poorly correlates with the experimental data, $R_{MM-PBSA} = 0.32 \pm 0.29$, as agreed in the recent outcomes.[84]

Atomistic simulations also revealed that the vdW interaction rigidly dominates the cou interaction during the binding process of inhibitors to the SARS-CoV-2 Mpro. Moreover, the residues *Thr26, His41, Ser46, Asn142, Gly143, Cys145, His164, Glu166,* and *Gln189* play essential roles in frequently forming NBC and HB to inhibitors.

ASSOCIATED CONTENT

Ⓢ Supporting Information

The Supporting Information is available free of charge at https://pubs.acs.org/doi/10.1021/acs.jcim.1c00159.

Details of free energy approach as well as FPL, LIE, MM-PBSA, and FEP approaches; FEP starting conformations of the SARS-CoV-2 Mpro + inhibitor complex and isolated inhibitor in solution; comparison between ligand−interaction diagram from Vina and AD4 calculations; python codes of ROC calculation and bootstrapping analysis; FPL, FPL refined, LIE, MM-PBSA, and FEP results in comparison with the experimental data; ROC-AUC results; comparison of AD4 and experimental binding poses of 11a, 11b, 13b, and boceprevir to SARS-CoV-2 Mpro; pulling force upon FPL simulations; all-atom RMSD of the SARS-CoV-2 Mpro + inhibitor complex and isolated inhibitor in solution; superposition between the distribution of all-atom RMSD of SARS-CoV-2 Mpro in the current work with the simulation data from RIKEN BDR; and residues forming NBC and HB to inhibitors (PDF)

■ AUTHOR INFORMATION

Corresponding Author

Son Tung Ngo − *Laboratory of Theoretical and Computational Biophysics, Ton Duc Thang University, Ho Chi Minh City 700000, Vietnam; Faculty of Applied Sciences, Ton Duc Thang University, Ho Chi Minh City 700000, Vietnam;* ⓞ orcid.org/0000-0003-1034-1768; Email: ngosontung@tdtu.edu.vn

Authors

Nguyen Minh Tam − *Faculty of Applied Sciences and Computional Chemistry Research Group, Ton Duc Thang University, Ho Chi Minh City 700000, Vietnam*

Minh Quan Pham − *Graduate University of Science and Technology and Institute of Natural Products Chemistry, Vietnam Academy of Science and Technology, Hanoi 100000, Vietnam;* ⓞ orcid.org/0000-0001-6922-1627

Trung Hai Nguyen − *Laboratory of Theoretical and Computational Biophysics, Ton Duc Thang University, Ho Chi Minh City 700000, Vietnam; Faculty of Applied Sciences, Ton Duc Thang University, Ho Chi Minh City 700000, Vietnam;* ⓞ orcid.org/0000-0003-1848-3963

Complete contact information is available at:
https://pubs.acs.org/10.1021/acs.jcim.1c00159

Author Contributions

All authors designed the studies, collected and analyzed the data, and wrote the manuscript.

Notes

The authors declare no competing financial interest.
All relevant data necessary to reproduce all results in the paper are within the main text and the Supporting Information. The input files for running calculations and computer code for doing analysis are included in the Supporting Information.

■ REFERENCES

(1) WHO. *Coronavirus Disease 2019 (COVID-19) Situation Report—52*, 2020.

(2) Huang, C.; Wang, Y.; Li, X.; Ren, L.; Zhao, J.; Hu, Y.; Zhang, L.; Fan, G.; Xu, J.; Gu, X.; Cheng, Z.; Yu, T.; Xia, J.; Wei, Y.; Wu, W.; Xie, X.; Yin, W.; Li, H.; Liu, M.; Xiao, Y.; Gao, H.; Guo, L.; Xie, J.; Wang, G.; Jiang, R.; Gao, Z.; Jin, Q.; Wang, J.; Cao, B. Clinical features of patients infected with 2019 novel coronavirus in Wuhan, China. *Lancet* **2020**, *395*, 497−506.

(3) Wang, C.; Horby, P. W.; Hayden, F. G.; Gao, G. F. A novel coronavirus outbreak of global health concern. *Lancet* **2020**, *395*, 470−473.

(4) Chen, Y. W.; Yiu, C.-P.Y.; Wong, K.-Y. Prediction of the SARS-CoV-2 (2019-nCoV) 3C-like Protease (3CLpro) Structure: Virtual Screening Reveals Velpatasvir, Ledipasvir, and Other Drug Repurposing Candidates. *F1000Res* **2020**, *9*, 129.

(5) Chan, J. F.-W.; Yuan, S.; Kok, K.-H.; To, K. K.-W.; Chu, H.; Yang, J.; Xing, F.; Liu, J.; Yip, C. C.-Y.; Poon, R. W.-S.; Tsoi, H.-W.; Lo, S. K.-F.; Chan, K.-H.; Poon, V. K.-M.; Chan, W.-M.; Ip, J. D.; Cai, J.-P.; Cheng, V. C.-C.; Chen, H.; Hui, C. K.-M.; Yuen, K.-Y. A Familial Cluster of Pneumonia Associated with the 2019 Novel Coronavirus Indicating Person-to-Person Transmission: a Study of a Family Cluster. *Lancet* **2020**, *395*, 514−523.

(6) van Doremalen, N.; Bushmaker, T.; Morris, D. H.; Holbrook, M. G.; Gamble, A.; Williamson, B. N.; Tamin, A.; Harcourt, J. L.; Thornburg, N. J.; Gerber, S. I.; Lloyd-Smith, J. O.; de Wit, E.; Munster, V. J. Aerosol and Surface Stability of SARS-CoV-2 as Compared with SARS-CoV-1. *N. Engl. J. Med.* **2020**, *382*, 1564−1567.

(7) FDA Approves First Treatment for COVID-19. https://www.fda.gov/news-events/press-announcements/fda-approves-first-treatment-covid-19?fbclid=IwAR3jElh3p4H0YrLtL0o92OE931R6ygixc2edh3zPX4E6SL4AbmMFNu19q8U (accessed Oct 27, 2020).

(8) Cohen, J.; Kupferschmidt, K. The "very, very bad look" of remdesivir, the first FDA-approved COVID-19 drug. *Science News*; American Association for the Advancement of Science 2020.

(9) Holshue, M. L.; DeBolt, C.; Lindquist, S.; Lofy, K. H.; Wiesman, J.; Bruce, H.; Spitters, C.; Ericson, K.; Wilkerson, S.; Tural, A.; Diaz, G.; Cohn, A.; Fox, L.; Patel, A.; Gerber, S. I.; Kim, L.; Tong, S.; Lu, X.; Lindstrom, S.; Pallansch, M. A.; Weldon, W. C.; Biggs, H. M.; Uyeki, T. M.; Pillai, S. K. First Case of 2019 Novel Coronavirus in the United States. *N. Engl. J. Med.* **2020**, *382*, 929−936.

(10) Beigel, J. H.; Tomashek, K. M.; Dodd, L. E.; Mehta, A. K.; Zingman, B. S.; Kalil, A. C.; Hohmann, E.; Chu, H. Y.; Luetkemeyer, A.; Kline, S.; Lopez de Castilla, D.; Finberg, R. W.; Dierberg, K.; Tapson, V.; Hsieh, L.; Patterson, T. F.; Paredes, R.; Sweeney, D. A.; Short, W. R.; Touloumi, G.; Lye, D. C.; Ohmagari, N.; Oh, M.-d.; Ruiz-Palacios, G. M.; Benfield, T.; Fätkenheuer, G.; Kortepeter, M. G.; Atmar, R. L.; Creech, C. B.; Lundgren, J.; Babiker, A. G.; Pett, S.; Neaton, J. D.; Burgess, T. H.; Bonnett, T.; Green, M.; Makowski, M.; Osinusi, A.; Nayak, S.; Lane, H. C. Remdesivir for the Treatment of Covid-19 — Final Report. *N. Engl. J. Med.* **2020**, *383*, 1813.

(11) Schoeman, D.; Fielding, B. C. Coronavirus envelope protein: current knowledge. *Virology* **2019**, *16*, 69.

(12) Fauquet, C.; Fargette, D. International Committee on Taxonomy of Viruses and the 3,142 unassigned species. *Virology* **2005**, *2*, 64.

(13) Zhavoronkov, A.; Aladinskiy, V.; Zhebrak, A.; Zagribelnyy, B.; Terentiev, V.; Bezrukov, D. S.; Polykovskiy, D.; Shayakhmetov, R.; Filimonov, A.; Orekhov, P.; Yan, Y.; Popova, O.; Vanhaelen, Q.; Aliper, A.; Ivanenkov, Y. Potential COVID-2019 3C-like Protease Inhibitors Designed Using Generative Deep Learning Approaches. **2020**, chemrxiv:11829102.v2.

(14) Gao, K.; Nguyen, D. D.; Chen, J.; Wang, R.; Wei, G.-W. Repositioning of 8565 Existing Drugs for COVID-19. *J. Phys. Chem. Lett.* **2020**, *11*, 5373−5382.

(15) Weston, S.; Coleman, C. M.; Haupt, R.; Logue, J.; Matthews, K.; Li, Y.; Reyes, H. M.; Weiss, S. R.; Frieman, M. B. Broad anti-coronaviral activity of FDA approved drugs against SARS-CoV-2 in vitro and SARS-CoV in vivo. **2020**, bioRxiv:25.008482.

(16) Ngo, S. T.; Quynh Anh Pham, N.; Thi Le, L.; Pham, D.-H.; Vu, V. V. Computational Determination of Potential Inhibitors of SARS-CoV-2 Main Protease. *J. Chem. Inf. Model.* **2020**, *60*, 5771−5780.

(17) Pham, M. Q.; Vu, K. B.; Han Pham, T. N.; Thuy Huong, L. T.; Tran, L. H.; Tung, N. T.; Vu, V. V.; Nguyen, T. H.; Ngo, S. T. Rapid prediction of possible inhibitors for SARS-CoV-2 main protease using docking and FPL simulations. *RSC Adv.* **2020**, *10*, 31991−31996.

(18) Ngo, S. T.; Nguyen, H. M.; Thuy Huong, L. T.; Quan, P. M.; Truong, V. K.; Tung, N. T.; Vu, V. V. Assessing potential inhibitors of SARS-CoV-2 main protease from available drugs using free energy perturbation simulations. *RSC Adv.* **2020**, *10*, 40284−40290.

(19) Marshall, G. R. Computer-Aided Drug Design. *Annu. Rev. Pharmacol. Toxicol.* **1987**, *27*, 193−213.

(20) Homeyer, N.; Stoll, F.; Hillisch, A.; Gohlke, H. Binding Free Energy Calculations for Lead Optimization: Assessment of Their Accuracy in an Industrial Drug Design Context. *J. Chem. Theory Comput.* **2014**, *10*, 3331−3344.

(21) Yu, W.; MacKerell, A. D. Computer-Aided Drug Design Methods. In *Antibiotics: Methods and Protocols*; Sass, P., Ed.; Springer New York: New York, NY, 2017; pp 85−106.

(22) Ngo, S. T.; Nguyen, T. H.; Tung, N. T.; Nam, P. C.; Vu, K. B.; Vu, V. V. Oversampling Free Energy Perturbation Simulation in Determination of the Ligand-Binding Free Energy. *J. Comput. Chem.* **2020**, *41*, 611−618.

(23) Decherchi, S.; Cavalli, A. Thermodynamics and Kinetics of Drug-Target Binding by Molecular Simulation. *Chem. Rev.* **2020**, *120*, 12788.

(24) Yang, J.; Chen, J. QSAR Analysis of Purine-Type and Propafenone-Type Substrates of P-Glycoprotein Targeting β-Amyloid Clearance. *Neurodegenerative Diseases*; Books on Demand, 2013; p 257.

(25) Trott, O.; Olson, A. J. AutoDock Vina: improving the speed and accuracy of docking with a new scoring function, efficient optimization, and multithreading. *J. Comput. Chem.* **2010**, *31*, 455−461.

(26) Batra, R.; Chan, H.; Kamath, G.; Ramprasad, R.; Cherukara, M. J.; Sankaranarayanan, S. K. R. S. Screening of Therapeutic Agents for COVID-19 Using Machine Learning and Ensemble Docking Studies. *J. Phys. Chem. Lett.* **2020**, *11*, 7058−7065.

(27) Hansson, T.; Marelius, J.; Åqvist, J. Ligand binding affinity prediction by linear interaction energy methods. *J. Comput.-Aided Mol. Des.* **1998**, *12*, 27−35.

(28) Ngo, S. T.; Hung, H. M.; Nguyen, M. T. Fast and Accurate Determination of the Relative Binding Affinities of Small Compounds to HIV-1 Protease using Non-Equilibrium Work. *J. Comput. Chem.* **2016**, *37*, 2734−2742.

(29) Srinivasan, J.; Cheatham, T. E.; Cieplak, P.; Kollman, P. A.; Case, D. A. Continuum Solvent Studies of the Stability of DNA, RNA, and Phosphoramidate−DNA Helices. *J. Am. Chem. Soc.* **1998**, *120*, 9401−9409.

(30) Kollman, P. A.; Massova, I.; Reyes, C.; Kuhn, B.; Huo, S.; Chong, L.; Lee, M.; Lee, T.; Duan, Y.; Wang, W.; Donini, O.; Cieplak, P.; Srinivasan, J.; Case, D. A.; Cheatham, T. E.. Calculating Structures and Free Energies of Complex Molecules: Combining Molecular Mechanics and Continuum Models. *Acc. Chem. Res.* **2000**, *33*, 889−897.

(31) Jarzynski, C. Equilibrium free-energy differences from non-equilibrium measurements: A master-equation approach. *Phys. Rev. E: Stat. Phys., Plasmas, Fluids, Relat. Interdiscip. Top.* **1997**, *56*, 5018−5035.

(32) Kollman, P. Free energy calculations: applications to chemical and biochemical phenomena. *Chem. Rev.* **1993**, *93*, 2395−2417.

(33) Zwanzig, R. W. High-Temperature Equation of State by a Perturbation Method. I. Nonpolar Gases. *J. Chem. Phys.* **1954**, *22*, 1420−1426.

(34) Nguyen, N. T.; Nguyen, T. H.; Pham, T. N. H.; Huy, N. T.; Bay, M. V.; Pham, M. Q.; Nam, P. C.; Vu, V. V.; Ngo, S. T. Autodock Vina Adopts More Accurate Binding Poses but Autodock4 Forms Better Binding Affinity. *J. Chem. Inf. Model.* **2020**, *60*, 204−211.

(35) Genheden, S.; Ryde, U. The MM/PBSA and MM/GBSA Methods to Estimate Ligand-Binding Affinities. *Expert Opin. Drug Discovery* **2015**, *10*, 449−461.

(36) Kuhn, B.; Kollman, P. A. Binding of a Diverse Set of Ligands to Avidin and Streptavidin: An Accurate Quantitative Prediction of Their Relative Affinities by a Combination of Molecular Mechanics and Continuum Solvent Models. *J. Med. Chem.* **2000**, *43*, 3786−3791.

(37) Schutz, C. N.; Warshel, A. What are the dielectric ?constants? of proteins and how to validate electrostatic models? *Proteins* **2001**, *44*, 400−417.

(38) Hou, T.; Guo, S.; Xu, X. Predictions of binding of a diverse set of ligands to Gelatinase-A by a combination of molecular dynamics and continuum solvent models. *J. Phys. Chem. B* **2002**, *106*, 5527−5535.

(39) Genheden, S.; Ryde, U. Comparison of end-point continuum-solvation methods for the calculation of protein-ligand binding free energies. *Proteins* **2012**, *80*, 1326−1342.

(40) Uciechowska, U.; Schemies, J.; Scharfe, M.; Lawson, M.; Wichapong, K.; Jung, M.; Sippl, W. Binding free energy calculations and biological testing of novel thiobarbiturates as inhibitors of the human NAD+ dependent histone deacetylase Sirt2. *MedChemComm* **2012**, *3*, 167−173.

(41) Morris, G. M.; Huey, R.; Lindstrom, W.; Sanner, M. F.; Belew, R. K.; Goodsell, D. S.; Olson, A. J. AutoDock4 and AutoDockTools4: Automated docking with selective receptor flexibility. *J. Comput. Chem.* **2009**, *30*, 2785−2791.

(42) Andi, B.; Kumaran, D.; Kreitler, D. F.; Soares, A. S.; Shi, W.; Jakoncic, J.; Fuchs, M. R.; Keereetaweep, J.; Shanklin, J.; McSweeney, S.Hepatitis C Virus NSP3/NSP4A Inhibitors as Promising Lead Compounds for the Design of New Covalent Inhibitors for SARS-CoV-2 3CLpro/Mpro Protease (accessed Oct 04).

(43) Kim, S.; Thiessen, P. A.; Bolton, E. E.; Chen, J.; Fu, G.; Gindulyte, A.; Han, L.; He, J.; He, S.; Shoemaker, B. A.; Wang, J.; Yu, B.; Zhang, J.; Bryant, S. H. PubChem Substance and Compound databases. *Nucleic Acids Res.* **2016**, *44*, D1202−D1213.

(44) Rathnayake, A. D.; Zheng, J.; Kim, Y.; Perera, K. D.; Mackin, S.; Meyerholz, D. K.; Kashipathy, M. M.; Battaile, K. P.; Lovell, S.; Perlman, S.; Groutas, W. C.; Chang, K.-O. 3C-like protease inhibitors block coronavirus replication in vitro and improve survival in MERS-CoV-infected mice. *Sci. Transl. Med.* **2020**, *12*, No. eabc5332.

(45) Dai, W.; Zhang, B.; Jiang, X.-M.; Su, H.; Li, J.; Zhao, Y.; Xie, X.; Jin, Z.; Peng, J.; Liu, F.; Li, C.; Li, Y.; Bai, F.; Wang, H.; Cheng, X.; Cen, X.; Hu, S.; Yang, X.; Wang, J.; Liu, X.; Xiao, G.; Jiang, H.; Rao, Z.; Zhang, L.-K.; Xu, Y.; Yang, H.; Liu, H. Structure-based Design of Antiviral Drug Candidates Targeting the SARS-CoV-2 Main Protease. *Science* **2020**, *368*, 1331−1335.

(46) Zhang, L.; Lin, D.; Sun, X.; Curth, U.; Drosten, C.; Sauerhering, L.; Becker, S.; Rox, K.; Hilgenfeld, R. Crystal structure of SARS-CoV-2 main protease provides a basis for design of improved α-ketoamide inhibitors. *Science* **2020**, *368*, 409−412.

(47) Su, H.-x.; Yao, S.; Zhao, W.-f.; Li, M.-j.; Liu, J.; Shang, W.-j.; Xie, H.; Ke, C.-q.; Hu, H.-c.; Gao, M.-n.; Yu, K.-q.; Liu, H.; Shen, J.-s.; Tang, W.; Zhang, L.-k.; Xiao, G.-f.; Ni, L.; Wang, D.-w.; Zuo, J.-p.; Jiang, H.-l.; Bai, F.; Wu, Y.; Ye, Y.; Xu, Y.-c. Anti-SARS-CoV-2 activities in vitro of Shuanghuanglian preparations and bioactive ingredients. *Acta Pharmacol. Sin.* **2020**, *41*, 1167−1177.

(48) Ma, C.; Sacco, M. D.; Hurst, B.; Townsend, J. A.; Hu, Y.; Szeto, T.; Zhang, X.; Tarbet, B.; Marty, M. T.; Chen, Y.; Wang, J. Boceprevir, GC-376, and calpain inhibitors II, XII inhibit SARS-CoV-2 viral replication by targeting the viral main protease. *Cell Res.* **2020**, *30*, 678−692.

(49) Jin, Z.; Du, X.; Xu, Y.; Deng, Y.; Liu, M.; Zhao, Y.; Zhang, B.; Li, X.; Zhang, L.; Peng, C.; Duan, Y.; Yu, J.; Wang, L.; Yang, K.; Liu, F.; Jiang, R.; Yang, X.; You, T.; Liu, X.; Yang, X.; Bai, F.; Liu, H.; Liu, X.; Guddat, L. W.; Xu, W.; Xiao, G.; Qin, C.; Shi, Z.; Jiang, H.; Rao, Z.; Yang, H. Structure of Mpro from SARS-CoV-2 and Discovery of its Inhibitors. *Nature* **2020**, *582*, 289−293.

(50) Vuong, W.; Khan, M. B.; Fischer, C.; Arutyunova, E.; Lamer, T.; Shields, J.; Saffran, H. A.; McKay, R. T.; van Belkum, M. J.; Joyce, M. A.; Young, H. S.; Tyrrell, D. L.; Vederas, J. C.; Lemieux, M. J. Feline coronavirus drug inhibits the main protease of SARS-CoV-2 and blocks virus replication. *Nat. Commun.* **2020**, *11*, 4282.

(51) Jeon, S.; Ko, M.; Lee, J.; Choi, I.; Byun, S. Y.; Park, S.; Shum, D.; Kim, S. Identification of Antiviral Drug Candidates against SARS-CoV-2 from FDA-Approved Drugs. *Antimicrob. Agents Chemother.* **2020**, *64*, e00819−20.

(52) Ngo, S. T.; Quynh Anh Pham, N.; Thi Le, L.; Pham, D.-H.; Vu, V. V. Computational Determination of Potential Inhibitors of SARS-CoV-2 Main Protease. *J. Chem. Inf. Model.* **2020**, *60*, 5771.

(53) Abraham, M. J.; Murtola, T.; Schulz, R.; Páll, S.; Smith, J. C.; Hess, B.; Lindahl, E. GROMACS: High Performance Molecular Simulations through Multi-Level Parallelism from Laptops to Supercomputers. *SoftwareX* **2015**, *1−2*, 19−25.

(54) Aliev, A. E.; Kulke, M.; Khaneja, H. S.; Chudasama, V.; Sheppard, T. D.; Lanigan, R. M. Motional Timescale Predictions by Molecular Dynamics Simulations: Case Study using Proline and Hydroxyproline Sidechain Dynamics. *Proteins: Struct., Funct., Bioinf.* **2014**, *82*, 195−215.

(55) Jorgensen, W. L.; Chandrasekhar, J.; Madura, J. D.; Impey, R. W.; Klein, M. L. Comparison of Simple Potential Functions for Simulating Liquid Water. *J. Chem. Phys.* **1983**, *79*, 926−935.

(56) Kim, M. O.; McCammon, J. A. Computation of pH-dependent binding free energies. *Biopolymers* **2016**, *105*, 43−49.

(57) Wang, J.; Wolf, R. M.; Caldwell, J. W.; Kollman, P. A.; Case, D. A. Development and Testing of a General Amber Force Field. *J. Comput. Chem.* **2004**, *25*, 1157−1174.

(58) Case, D. A.; Ben-Shalom, I. Y.; Brozell, S. R.; Cerutti, D. S.; Cheatham, T. E.; Cruzeiro, V. W. D., III; Darden, T. A.; Duke, R. E.; Ghoreishi, D.; Gilson, M. K.; Gohlke, H.; Goetz, A. W.; Greene, D.; Harris, R.; Homeyer, N.; Huang, Y.; Izadi, S.; Kovalenko, A.; Kurtzman, T.; Lee, T. S.; LeGrand, S.; Li, P.; Lin, C.; Liu, J.; Luchko, T.; Luo, R.; Mermelstein, D. J.; Merz, K. M.; Miao, Y.; Monard, G.; Nguyen, C.; Nguyen, H.; Omelyan, I.; Onufriev, A.; Pan, F.; Qi, R.; Roe, D. R.; Roitberg, A.; Sagui, C.; Schott-Verdugo, S.; Shen, J.; Simmerling, C. L.; Smith, J.; SalomonFerrer, R.; Swails, J.; Walker, R. C.; Wang, J.; Wei, H.; Wolf, R. M.; Wu, X.; Xiao, L.; York, D. M.; Kollman, P. A. *AMBER 18*; University of California: San Francisco, 2018.

(59) Sousa da Silva, A. W.; Vranken, W. F. ACPYPE - AnteChamber PYthon Parser interfacE. *BMC Res. Notes* **2012**, *5*, 367.

(60) Darden, T.; York, D.; Pedersen, L. Particle mesh Ewald: AnN·log(N) method for Ewald sums in large systems. *J. Chem. Phys.* **1993**, *98*, 10089−10092.

(61) Park, S.; Schulten, K. Calculating Potentials of Mean Force from Steered Molecular Dynamics Simulations. *J. Chem. Phys.* **2004**, *120*, 5946−5961.

(62) Almlöf, M.; Brandsdal, B. O.; Åqvist, J. Binding affinity prediction with different force fields: Examination of the linear interaction energy method. *J. Comput. Chem.* **2004**, *25*, 1242−1254.

(63) Shrake, A.; Rupley, J. A. Environment and exposure to solvent of protein atoms. Lysozyme and insulin. *J. Mol. Biol.* **1973**, *79*, 351−371.

(64) Sitkoff, D.; Sharp, K. A.; Honig, B. Accurate calculation of hydration free energies using macroscopic solvent models. *J. Phys. Chem.* **1994**, *98*, 1978−1988.

(65) Sharp, K. A.; Honig, B. Electrostatic interactions in macromolecules: theory and applications. *Annu. Rev. Biophys. Biophys. Chem.* **1990**, *19*, 301−332.

(66) Baker, N. A.; Sept, D.; Joseph, S.; Holst, M. J.; McCammon, J. A. Electrostatics of Nanosystems: Application to Microtubules and the Ribosome. *Proc. Natl. Acad. Sci. U.S.A.* **2001**, *98*, 10037−10041.

(67) McQuarrie, D. A. *Statistical Thermodynamics*; Harper and Row: New York, 1973.

(68) Ytreberg, F. M. Absolute FKBP binding affinities obtained via nonequilibrium unbinding simulations. *J. Chem. Phys.* **2009**, *130*, 164906.

(69) Bennett, C. H. Efficient estimation of free energy differences from Monte Carlo data. *J. Comput. Phys.* **1976**, *22*, 245−268.

(70) Henderson, J. A.; Harris, R. C.; Tsai, C.-C.; Shen, J. How Ligand Protonation State Controls Water in Protein-Ligand Binding. *J. Phys. Chem. Lett.* **2018**, *9*, 5440−5444.

(71) Dolinsky, T. J.; Czodrowski, P.; Li, H.; Nielsen, J. E.; Jensen, J. H.; Klebe, G.; Baker, N. A. PDB2PQR: expanding and upgrading automated preparation of biomolecular structures for molecular simulations. *Nucleic Acids Res.* **2007**, *35*, W522−W525.

(72) Efron, B. Bootstrap Methods: Another Kook at the Jackknife. *Ann. Stat.* **1979**, *7*, 1−26.

(73) Pedregosa, F.; Varoquaux, G.; Gramfort, A.; Michel, V.; Thirion, B.; Grisel, O.; Blondel, M.; Prettenhofer, P.; Weiss, R.; Dubourg, V.; Vanderplas, J.; Passos, A.; Cournapeau, D.; Brucher, M.; Perrot, M.; Duchesnay, E. Scikit-learn: Machine Learning in Python. *J. Mach. Learn. Res.* **2011**, *12*, 2825−2830.

(74) Macchiagodena, M.; Pagliai, M.; Karrenbrock, M.; Guarnieri, G.; Iannone, F.; Procacci, P. Virtual Double-System Single-Box: A Nonequilibrium Alchemical Technique for Absolute Binding Free Energy Calculations: Application to Ligands of the SARS-CoV-2 Main Protease. *J. Chem. Theor. Comput.* **2020**, *16*, 7160−7172.

(75) Günther, S.; Reinke, P. Y. A.; Fernández-García, Y.; Lieske, J.; Lane, T. J.; Ginn, H. M.; Koua, F. H. M.; Ehrt, C.; Ewert, W.; Oberthuer, D.; Yefanov, O.; Meier, S.; Lorenzen, K.; Krichel, B.; Kopicki, J.-D.; Gelisio, L.; Brehm, W.; Dunkel, I.; Seychell, B.; Gieseler, H.; Norton-Baker, B.; Escudero-Pérez, B.; Domaracky, M.; Saouane, S.; Tolstikova, A.; White, T. A.; Hänle, A.; Groessler, M.; Fleckenstein, H.; Trost, F.; Galchenkova, M.; Gevorkov, Y.; Li, C.; Awel, S.; Peck, A.; Barthelmess, M.; Schlünzen, F.; Xavier, P. L.; Werner, N.; Andaleeb, H.; Ullah, N.; Falke, S.; Srinivasan, V.; Franca, B. A.; Schwinzer, M.; Brognaro, H.; Rogers, C.; Melo, D.; Zaitsev-Doyle, J. J.; Knoska, J.; Peña Murillo, G. E.; Mashhour, A. R.; Guicking, F.; Hennicke, V.; Fischer, P.; Hakanpää, J.; Meyer, J.; Gribbon, P.; Ellinger, B.; Kuzikov, M.; Wolf, M.; Beccari, A. R.; Bourenkov, G.; Stetten, D. v.; Pompidor, G.; Bento, I.; Panneerselvam, S.; Karpics, I.; Schneider, T. R.; Garcia Alai, M. M.; Niebling, S.; Günther, C.; Schmidt, C.; Schubert, R.; Han, H.; Boger, J.; Monteiro, D. C. F.; Zhang, L.; Sun, X.; Pletzer-Zelgert, J.; Wollenhaupt, J.; Feiler, C. G.; Weiss, M. S.; Schulz, E.-C.; Mehrabi, P.; Karničar, K.; Usenik, A.; Loboda, J.; Tidow, H.; Chari, A.; Hilgenfeld, R.; Uetrecht, C.; Cox, R.; Zaliani, A.; Beck, T.; Rarey, M.; Günther, S.; Turk, D.; Hinrichs, W.; Chapman, H. N.; Pearson, A. R.; Betzel, C.; Meents, A., Inhibition of SARS-CoV-2 Main Protease by Allosteric Drug-Binding. **2020**, bioRxiv:12.378422.

(76) Komatsu, T. S.; Koyama, Y.; Okimoto, N.; Morimoto, G.; Ohno, Y.; Taiji, M. COVID-19 related trajectory data of 10 microseconds all atom molecular dynamics simulation of SARS-CoV-2 dimeric main protease. *Mendeley Data*; 2020.

(77) Bjelic, S.; Nervall, M.; Gutiérrez-de-Terán, H.; Ersmark, K.; Hallberg, A.; Åqvist, J. Computational inhibitor design against malaria plasmepsins. *Cell. Mol. Life Sci.* **2007**, *64*, 2285−2305.

(78) Ngo, S. T.; Mai, B. K.; Derreumaux, P.; Vu, V. V. Adequate prediction for inhibitor affinity of Aβ40 protofibril using the linear interaction energy method. *RSC Adv.* **2019**, *9*, 12455−12461.

(79) Zhang, H.; Yin, C.; Jiang, Y.; van der Spoel, D. Force Field Benchmark of Amino Acids: I. Hydration and Diffusion in Different Water Models. *J. Chem. Inf. Model.* **2018**, *58*, 1037−1052.

(80) Zhang, H.; Jiang, Y.; Cui, Z.; Yin, C. Force Field Benchmark of Amino Acids. 2. Partition Coefficients between Water and Organic Solvents. *J. Chem. Inf. Model.* **2018**, *58*, 1669−1681.

(81) Viet, M. H.; Ngo, S. T.; Lam, N. S.; Li, M. S. Inhibition of Aggregation of Amyloid Peptides by Beta-Sheet Breaker Peptides and Their Binding Affinity. *J. Phys. Chem. B* **2011**, *115*, 7433−7446.

(82) Ngo, S. T.; Li, M. S. Curcumin Binds to Aβ1-40 Peptides and Fibrils Stronger Than Ibuprofen and Naproxen. *J. Phys. Chem. B* **2012**, *116*, 10165−10175.

(83) Ngo, S. T.; Hung, H. M.; Truong, D. T.; Nguyen, M. T. Replica Exchange Molecular Dynamics Study of the Truncated Amyloid Beta (11-40) Trimer in Solution. *Phys. Chem. Chem. Phys.* **2017**, *19*, 1909−1919.

(84) Li, Z.; Li, X.; Huang, Y.-Y.; Wu, Y.; Liu, R.; Zhou, L.; Lin, Y.; Wu, D.; Zhang, L.; Liu, H.; Xu, X.; Yu, K.; Zhang, Y.; Cui, J.; Zhan, C.-G.; Wang, X.; Luo, H.-B. Identify Potent SARS-CoV-2 Main Protease Inhibitors via Accelerated Free Energy Perturbation-Based Virtual Screening of Existing Drugs. *Proc. Natl. Acad. Sci. U.S.A.* **2020**, *117*, 27381−27387.

(85) Hou, T.; Wang, J.; Li, Y.; Wang, W. Assessing the Performance of the MM/PBSA and MM/GBSA Methods. 1. The Accuracy of Binding Free Energy Calculations Based on Molecular Dynamics Simulations. *J. Chem. Inf. Model.* **2011**, *51*, 69−82.

(86) Ryde, U.; Söderhjelm, P. Ligand-Binding Affinity Estimates Supported by Quantum-Mechanical Methods. *Chem. Rev.* **2016**, *116*, 5520−5566.

(87) Mondal, D.; Warshel, A. Exploring the Mechanism of Covalent Inhibition: Simulating the Binding Free Energy of α-Ketoamide Inhibitors of the Main Protease of SARS-CoV-2. *Biochem* **2020**, *59*, 4601−4608.

(88) Arafet, K.; Serrano-Aparicio, N.; Lodola, A.; Mulholland, A. J.; González, F. V.; Świderek, K.; Moliner, V. Mechanism of inhibition of SARS-CoV-2 Mpro by N3 peptidyl Michael acceptor explained by QM/MM simulations and design of new derivatives with tunable chemical reactivity. *Chem. Sci.* **2021**, *12*, 1433.

(89) Ramos-Guzmán, C. A.; Ruiz-Pernía, J. J.; Tuñón, I. Multiscale Simulations of SARS-CoV-2 3CL Protease Inhibition with Aldehyde Derivatives. Role of Protein and Inhibitor Conformational Dynamics in the Reaction Mechanism. *ACS Catal.* **2021**, *11*, 4157.